

# Analysis of deep sub-micron resolution in microsphere based imaging

Cite as: Appl. Phys. Lett. **105**, 204102 (2014); <https://doi.org/10.1063/1.4902247>

Submitted: 07 October 2014 . Accepted: 10 November 2014 . Published Online: 17 November 2014

Vijay M. Sundaram, and Sy-Bor Wen



View Online



Export Citation



CrossMark

## ARTICLES YOU MAY BE INTERESTED IN

[Advantages of microsphere-assisted super-resolution imaging technique over solid immersion lens and confocal microscopies](#)

Applied Physics Letters **104**, 061117 (2014); <https://doi.org/10.1063/1.4864760>

[Microsphere based microscope with optical super-resolution capability](#)

Applied Physics Letters **99**, 203102 (2011); <https://doi.org/10.1063/1.3662010>

[Optical super-resolution by high-index liquid-immersed microspheres](#)

Applied Physics Letters **101**, 141128 (2012); <https://doi.org/10.1063/1.4757600>



Webinar  
How to Characterize Magnetic Materials Using Lock-in Amplifiers

Zurich Instruments MFLI

Zurich Instruments

CRYOGENIC

Register now

## Analysis of deep sub-micron resolution in microsphere based imaging

Vijay M. Sundaram and Sy-Bor Wen<sup>a)</sup>

Department of Mechanical Engineering, Texas A&M University, College Station, Texas 77843, USA

(Received 7 October 2014; accepted 10 November 2014; published online 17 November 2014)

Based on full wave simulations,  $\sim 0.3\lambda$  and  $\sim 0.24\lambda$  imaging resolutions can be achieved for incoherent transverse and longitudinal point dipoles, respectively, when the dipoles are on an aluminum oxide base with a fused silica microsphere as the imaging lens. These high spatial resolutions (better than  $0.5\lambda$ ) can be attributed to almost  $90^\circ$  light acceptance angle of the microsphere and the solid immersion effects from the microsphere/base material. These simulation results can explain the  $\geq 0.3\lambda$  and  $\geq 0.24\lambda$  minimum resolvable center to center separation distance for thin metallic nanostructures and elongated metallic nanostructures, respectively, which is equal to  $\geq 0.1-0.14\lambda$  edge to edge distance observed in previous microsphere imaging experiments. © 2014 AIP Publishing LLC. [<http://dx.doi.org/10.1063/1.4902247>]

Better than  $\sim \lambda/4$  imaging resolution with dielectric microspheres in air has been reported by many groups recently, which is higher than the  $\sim \lambda/2$  resolution limit<sup>1-7</sup> and has a great potential for super-resolution microscopy required in nanoscience and molecular biology.<sup>8,9</sup> In most of the demonstrations, a silica microsphere of diameter  $\sim 4-50\mu\text{m}$  is placed on the target plane as the first lens. A high numerical aperture (NA) objective is placed along the imaging path of the microsphere to further magnify the real/virtual images from the microspheres.<sup>10</sup> Even with numerous successful demonstrations, the mechanisms providing the high spatial resolution with microspheres are still unclear. Compared with macroscale lenses, microspheres have larger curvature and corresponding almost zero front focal distance (FFD). As a result, the refractive index of the lens,  $n$ , can contribute to the spatial resolution of the target (i.e., solid immersion effect).<sup>11-13</sup> Also, due to the almost zero FFD, the acceptance angle of the microsphere from the target plane is  $\sim 90^\circ$ , which results in an effective numerical aperture  $\sim n$  when the microsphere is applied in the imaging.<sup>14</sup> In addition, since the microsphere is in direct contact with the target, the refractive index of the base material of the target can also affect the light diffraction and the associated imaging resolution.<sup>1,15</sup>

To verify the contribution of each mechanism to explain the 100 nm level (or better) spatial resolution reported in different groups, numerical experiments of the light propagation from the target through a microsphere, an objective lens and then to the imaging plane are performed in this study. Compared with the hand-on experiments, the numerical experiments allow us to adjust each parameter, including the polarization of light, independently to identify their contribution to the spatial resolution in microsphere based imaging. Description of the arrangement and conditions studied with the numerical experiments are as follows.

Full wave finite element method (FEM) simulation is adopted to identify the contributions of the refractive indices of microspheres, target and the polarization direction of the

collected light on the spatial resolution of a microsphere imaging system. Schematic of the simulation domain is shown in Fig. 1. A dipole (either x-y transverse or z longitudinal dipole) on the target plane with close proximity to the microsphere is selected as a point source on the target. In order to form a real image with the microsphere, a lens pair is placed above the microsphere to mimic the function of high numerical aperture objective lens in reported microsphere imaging experiments.<sup>9</sup> The lens pair can capture almost all the light from the microsphere to assure the optical resolution is mainly determined by the microsphere rather than the lens pair. The dielectric microsphere has a diameter of  $6\mu\text{m}$  which is the approximate average diameter that is commonly used in microsphere imaging experiments. The two lenses in the lens pair have diameters equal to  $20\mu\text{m}$  and  $40\mu\text{m}$  with refractive index  $n = 1.5$  and  $n = 1.4$ , respectively. The refractive index and diameter of the lens pair is selected to get the maximum possible magnification that can be achieved with the capable the simulation power. The position of the lens pair is adjusted such that the first lens collimates the light diffracted by the microsphere and the

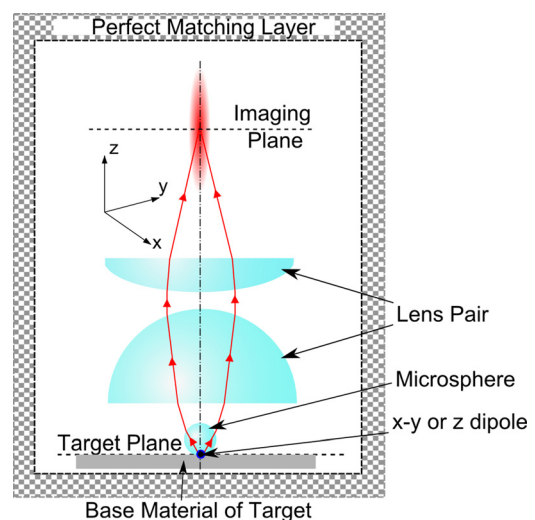


FIG. 1. Schematic of the simulation domain consisting of the target, microsphere, and lens pair.

<sup>a)</sup> Author to whom correspondence should be addressed. Electronic mail: syborwen@tamu.edu

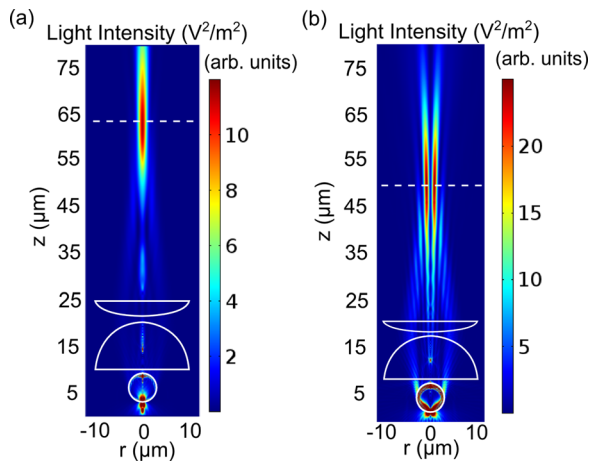


FIG. 2. Light intensity ( $\sim|E|^2$ ) distribution induced by (a) a transverse dipole (x-y dipole), and (b) a longitudinal dipole (z-dipole), in air with a microlens of diameter  $\sim 6 \mu\text{m}$  and refractive index  $n = 1.4$ . The dashed lines indicate the imaging plane.

second lens focuses the collimated light to form an image on its focal plane. To study the microsphere imaging at visible wavelengths,  $\lambda = 500 \text{ nm}$  is selected. The simulation domain is surrounded by a perfect matching layer to approximate an open domain. Triangular mesh elements with size less than  $\lambda/15$  are applied around the imaging plane. For other domains, the mesh size is less than  $\lambda/10$ . The size of the focus/image spot is determined by measuring the FWHM of light intensity (i.e., point spread function, PSF) at the imaging plane where the FWHM of the PSF achieves its minimum value (Fig. 2). The magnification ratio of the imaging system is determined by transverse displacement ratio between the PSF and the point dipole in the x direction when the dipole is away from the optical axis. The obtained magnification values are almost the same as the ratio between the backward focus numerical aperture (at target plane) and forward focus numerical aperture (at the imaging plane).<sup>16,17</sup> Since the microsphere is in contact with the target, the backward focus numerical aperture from the target to the microsphere is  $\sim n$  with  $n$  the refractive index of the microsphere. A two-point resolution criterion for point dipoles (i.e., minimum resolvable separation distance between two dipoles is equal to FWHM of PSF divided by the magnification ratio  $M$ ) is used to determine the point dipole spatial resolution in this study.<sup>17</sup>

#### (a) Refractive index of microsphere

The focal plane of a spherical lens is inside the lens when its refractive index  $n$  is larger than  $\sim 1.5$ . Therefore,  $n < 1.5$  is studied in this portion of analysis. A transverse dipole in air is selected as the point target. Light emitted from the transverse dipole, when collimated by the first lens of the lens pair in Fig. 1, resembles a linearly polarized Airy beam. The focus/image spot of a linearly polarized Airy beam is not axisymmetric: larger FWHM in the polarization direction (Fig. 3(a)). This difference becomes smaller for larger magnification ratio. Due to the limited simulation power, the magnification ratio of the entire imaging system is limited to  $< 10$  to prevent oversized simulation. Table I lists the obtained FWHM of the PSF, magnification  $M$ , and the dipole resolution at the imaging plane (i.e., FWHM of the PSF divided by  $M$ ) with refractive index of the microsphere  $n = 1.3, 1.35, 1.4, \text{ and } 1.45$ . Based on the results, the imaging resolution improves with increase in refractive index of the microsphere. The best imaging resolution is  $\sim 0.38 \lambda$  in the direction normal to the polarization which happens when  $n = 1.45$  under the magnification ratio studied. The improvement in resolution with refractive index of the microsphere can be attributed to solid immersion effect of the microsphere. The high refractive index of the microsphere, compared with air, results in the coupling of higher spatial frequency components ( $2\pi/\lambda < k < 2\pi n/\lambda$ ) from the emitter to the far field through the microsphere, thereby increasing the imaging resolution.

#### (b) Refractive index of base material of the target

Fused silica (FS) with refractive index 1.45 and aluminum oxide (AO) with refractive index 1.77, which are the two common target base materials in published microsphere imaging experiments, are selected in this portion of analysis to identify the contributions of the refractive index of the base material of the target on the microsphere imaging resolution with  $n = 1.45$ . A lens pair is placed on top of the microsphere to generate real images on the image plane. A transverse dipole is again selected as a point source on the target as in the previous analysis. Each target has a thickness  $\sim 2 \lambda$  to prevent the interference from the bottom surface of the target during the imaging process. Table II lists the simulated FWHM of the PSF, magnification  $M$ , and the dipole resolution at the imaging plane of the microsphere based imaging system when the transverse point dipole is placed

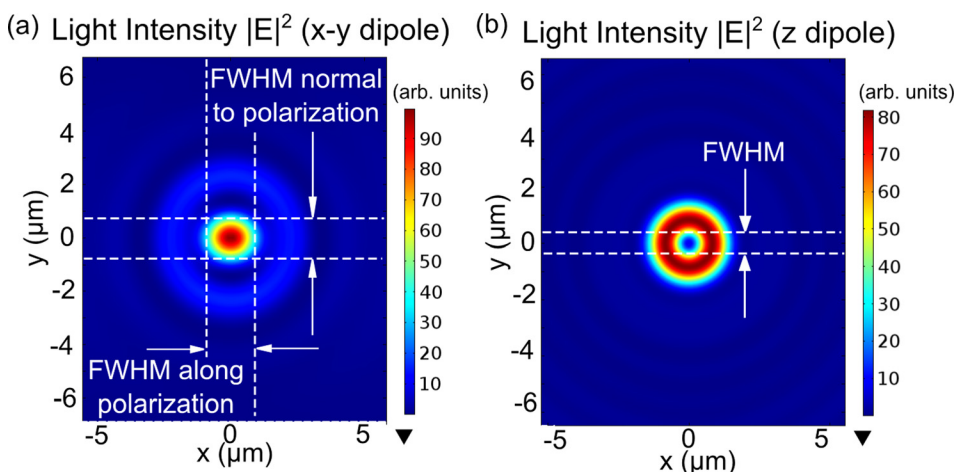


FIG. 3. Light intensity distribution at the image plane of (a) a transverse dipole (i.e., x-y dipole) and (b) a longitudinal dipole (i.e., z dipole).

TABLE I. Simulated FWHM of the PSF, magnification M, and the dipole resolution at the imaging plane of the microsphere based imaging system for different refractive index of the microsphere.

n	FWHM of the PSF ( $\parallel/\perp$ ) ( $\mu\text{m}/\mu\text{m}$ )	M	Dipole spatial resolution ( $\parallel/\perp$ ) (nm/nm)	Resolution in terms of $\lambda$ ( $\parallel/\perp$ )
1.3	1.54/1.32	6.1	252/216	$0.51\lambda/0.43\lambda$
1.35	1.59/1.33	6.4	248/208	$0.5\lambda/0.42\lambda$
1.4	1.66/1.38	6.8	244/203	$0.49\lambda/0.4\lambda$
1.45	1.7/1.4	7.2	236/194	$0.47\lambda/0.38\lambda$

on selected targets. For both AO and FS as the target material, the obtained dipole spatial resolution is better than that in air. Among AO and FS, AO with a higher refractive index provides a slightly better resolution for the transverse point dipoles placed on top of it. The improvement in the spatial resolution can be considered as a solid immersion effect from the target which does not happen in regular far field imaging with macroscale lenses far away from the target.

(c) *Polarization of the emitter*

In this portion of the analysis, a longitudinal dipole (or z-dipole) rather than a transverse dipole (or x-y dipole) is selected as the emitter to be imaged by the microsphere. The light emitted from a longitudinal dipole is radially polarized similar to diffraction free Bessel beams.<sup>18</sup> The light intensity distribution of the radially polarized beam has a doughnut shape at the focal/image spot with low numerical aperture (i.e.,  $\text{NA} < 0.8$ ) lenses. The doughnut shape intensity distribution arises due to the dominant transverse fields at low NA which have a phase singularity at the center of the beam.<sup>19</sup> Due to the low numerical aperture of most imaging lenses, the PSF of a longitudinal dipole at the imaging plane has a symmetric doughnut shape intensity distribution. The FWHM of the doughnut shaped PSF is defined as FWHM of the central hole in the doughnut intensity distribution obtained at the imaging plane as indicated in Fig. 3(b). Table III lists the simulated FWHM of the PSF, magnification M, and the dipole resolution at the imaging plane of the microsphere based imaging system when the longitudinal point dipole is placed on selected targets (air, FS, and AO). The imaging resolution of the longitudinal dipole with a microsphere follows the same trend as that with the transverse dipole, i.e., the highest resolution occurs when the dipole is placed on the AO target ( $\sim 0.24\lambda$ ) due to the high refractive index and the associated stronger solid immersion effect. Compared with transverse point dipole, longitudinal point dipole provides better spatial resolution under the same

TABLE II. Simulated FWHM of the PSF, magnification M, and the dipole resolution at the imaging plane of the microsphere based imaging system when the transverse point dipole is placed on different targets.

Base material of target	FWHM of the PSF ( $\parallel/\perp$ ) ( $\mu\text{m}/\mu\text{m}$ )	M	Dipole spatial resolution ( $\parallel/\perp$ ) (nm/nm)	Resolution in terms of $\lambda$ ( $\parallel/\perp$ )
Air	1.73/1.4	7.2	236/194	$0.47\lambda/0.38\lambda$
AO	1.3/1.19	7.6	171/156	$0.34\lambda/0.3\lambda$
FS	1.56/1.3	7.4	210/175	$0.42\lambda/0.35\lambda$

TABLE III. Simulated FWHM of the PSF, magnification M, and the dipole resolution at the imaging plane of the microsphere based imaging system when the longitudinal point dipole is placed on different targets.

Base material of target	FWHM of the PSF (nm)	M	Dipole spatial resolution (nm)	Resolution in terms of $\lambda$
Air	860	6	143	$0.28\lambda$
AO	790	6.6	120	$0.24\lambda$
FS	840	6.4	131	$0.26\lambda$

microsphere and target conditions. The higher resolution with the longitudinal dipole can be attributed to the increased amplitude of higher spatial frequency components collected by the microsphere and the correspondingly larger effective collecting angle (Fig. 2(b)) when it is compared with a transverse dipole (Fig. 2(a)). Note that due to the smaller acceptance angle ( $\leq 70^\circ$ ) of most far-field objective lenses, the emission from the longitudinal dipole cannot be effectively captured with far-field macroscale lenses compared with near field microlenses as in the microsphere imaging.

From the discussion in the above paragraphs, it can be concluded that the best achievable resolution for incoherent point sources with dielectric microsphere of  $n = 1.45$  and diameter of  $6\mu\text{m}$  (used in many microsphere imaging experiments) is  $\sim 0.3\lambda$  for transverse point dipole and  $\sim 0.24\lambda$  for longitudinal point dipole on an AO target. In a real imaging process, emitters are finite size nanostructures. Radiation from each location of a finite size nanostructure under reflected or transmitted illumination may not be incoherent as assumed in many publications. To verify the coherence of emission from finite size emitters, FEM simulation is conducted to study the electric field phase distribution in gold nanostructures of different widths. Two types of nanostructures are examined, namely, a thin film gold nanostructure of thickness  $\sim 30\text{nm}$  (around the skin depth of gold) (Fig. 4(a)) and an elongated gold nanostructure (i.e., width much less than the thickness) of thickness  $\sim \lambda$  (Fig. 4(b)). Both nanostructures can be fabricated with available techniques and are commonly used in microsphere imaging experiments. The nanostructures are exposed to linearly polarized illumination along the x-z plane from an external lens with a  $\text{NA} \sim 0.7$ . The nanostructures are  $\sim 1\mu\text{m}$  before focal point of the external illumination. The nanostructures are displaced  $\sim 250\text{nm}$  away from the optical axis, which is around the middle between the center and the edge of the illumination region. For the thin film nanostructure with a thickness  $\sim 30\text{nm}$ , it is observed from the simulation that the electric field inside the nanostructure is mainly in the transverse direction (i.e.,  $E_x \geq 10 E_z$ ) (Fig. 4(a)). Also observed is that the electron oscillation inside the thin film gold nanostructure is almost spatially coherent (within  $15^\circ$  of phase lag<sup>20</sup>) when the width of the nanostructure is  $\leq 0.2\lambda$ . Hence, the induced re-emission from a gold thin film nanostructure of width  $\leq 0.2\lambda$  under an external illumination is similar to emission from a finite size transverse dipole with its length equal to the width of the nanostructure. Since the image spread function of a finite size transverse dipole with a width  $\leq 0.2\lambda$  is equal to the point spread function of a point transverse dipole on the image plane, the image pattern of two

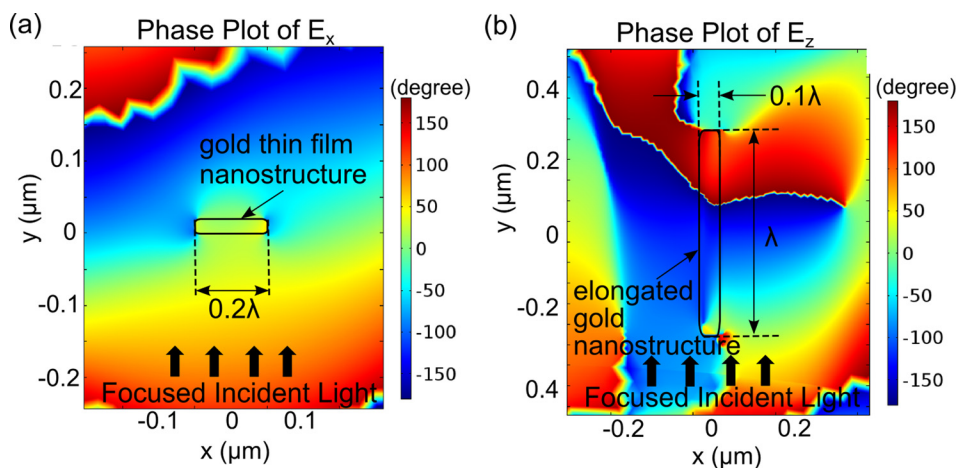


FIG. 4. Phase plot of x component of electric field when focused light (NA  $\sim 0.7$ ) is incident on a gold thin film nanostructure with a width  $\sim 0.2\lambda$  and thickness  $\sim 30$  nm. (b) Phase plot of z component of electric field when focused light (NA  $\sim 0.7$ ) is incident on an elongated gold nanostructure with a width  $\sim 0.1\lambda$  and thickness  $\sim \lambda$ .

thin film gold nanostructures with width less than  $0.2\lambda$  is the same as two point transverse dipoles located at the center of the two thin film nanostructures. Therefore, for any gold thin film nanostructure with a width less than  $0.2\lambda$ , the minimum resolvable “center to center” separation distance of the nanostructure on AO is  $\sim 0.3\lambda$  as determined in Table II. This statement can be used to explain the reported  $\geq 0.1\lambda$  “edge to edge” resolution in microsphere imaging results with thin film gold nano-patterns.<sup>4,10</sup>

For the elongated nanostructure with a thickness  $\sim \lambda$ , it is observed from the similar simulation that the electric field inside the nanostructure is mainly in the longitudinal direction (i.e.,  $E_z \geq 5 E_x$ ) (Fig. 4(b)). The electron oscillation inside the elongated nanostructure is almost spatially coherent when the width of the nanostructure is  $\leq 0.1\lambda$ . Hence, the induced re-emission from an elongated gold nanostructure of width  $\leq 0.1\lambda$  under an external illumination is similar to emission from a finite size longitudinal dipole (with length equal to the thickness of the nanostructure). Since the image spread function of a finite size longitudinal dipole (with infinitely small width) is equal to the point spread function of a point longitudinal dipole (also infinitely small width) on the image plane, the image pattern of two elongated gold nanostructures with width less than  $0.1\lambda$  is the same as two point longitudinal dipoles located at the center of the two elongated nanostructures. Therefore, for any elongated gold nanostructure with a width less than  $0.1\lambda$ , the minimum resolvable “center to center” separation distance of the nanostructure on AO is  $\sim 0.24\lambda$  as determined in Table III, which corresponds to “edge to edge” resolvable separation distance  $\sim 0.14\lambda$ .

In conclusion, due to the almost  $90^\circ$  light acceptance angle of the microsphere as well as the solid immersion effect from the microsphere and the target, the highest spatial resolution in fused silica microsphere imaging for point sources on an AO target is  $\sim 0.3\lambda$  for transverse dipole and  $\sim 0.24\lambda$  for longitudinal dipole imaged. These imaging resolutions correspond to (a) minimum resolvable center to center separation distance  $\sim 0.3\lambda$  for thin metallic nanostructure with a width  $\leq 0.2\lambda$ , which corresponds to edge to edge resolvable separation distance commonly reported in experiments as  $\sim 0.1\lambda$ ; and (b) minimum resolvable center to center separation distance  $\sim 0.24\lambda$  for elongated metallic

nanostructure with a width  $\leq 0.1\lambda$  when the nanostructures are on AO substrate, which corresponds to edge to edge resolvable separation distance commonly used in experiments as  $\sim 0.14\lambda$ .

This work was supported by National Science Foundation (CBET 0845794). The authors are pleased to acknowledge the Texas A&M Supercomputing Facility (<http://sc.tamu.edu/>) for providing the computing resources for this research.

- <sup>1</sup>Z. B. Wang, W. Guo, L. Li, B. Luk'yanchuk, A. Khan, Z. Liu, Z. C. Chen, and M. H. Hong, *Nat. Commun.* **2**, 218–224 (2011).
- <sup>2</sup>X. Hao, C. F. Kuang, X. Liu, H. J. Zhang, and Y. H. Li, *Appl. Phys. Lett.* **99**(20), 203102 (2011).
- <sup>3</sup>A. Vlad, I. Huynen, and S. Melinte, *Nanotechnology* **23**(28), 285708 (2012).
- <sup>4</sup>A. Darafsheh, G. F. Walsh, L. Dal Negro, and V. N. Astratov, *Appl. Phys. Lett.* **101**(14), 141128 (2012).
- <sup>5</sup>S. Lee, L. Li, Z. B. Wang, W. Guo, Y. Z. Yan, and T. Wang, *Appl. Opt.* **52**(30), 7265–7270 (2013).
- <sup>6</sup>Y. Z. Yan, L. Li, C. Feng, W. Guo, S. Lee, and M. H. Hong, *ACS Nano* **8**(2), 1809–1816 (2014).
- <sup>7</sup>X. Hao, C. F. Kuang, Z. T. Gu, Y. F. Wang, S. A. Li, Y. L. Ku, Y. H. Li, J. H. Ge, and X. Liu, *Light-Sci. Appl.* **2**, e102 (2013).
- <sup>8</sup>L. Li, W. Guo, Y. Z. Yan, S. Lee, and T. Wang, *Light-Sci. Appl.* **2**, e104 (2013).
- <sup>9</sup>H. Yang, N. Moullan, J. Auwerx, and M. A. M. Gijs, *Small* **10**(9), 1712–1718 (2014).
- <sup>10</sup>A. Darafsheh, N. I. Limberopoulos, J. S. Derov, D. E. Walker, and V. N. Astratov, *Appl. Phys. Lett.* **104**(6), 061117 (2014).
- <sup>11</sup>L. P. Ghislain and V. B. Elings, *Appl. Phys. Lett.* **72**(22), 2779–2781 (1998).
- <sup>12</sup>L. P. Ghislain, V. B. Elings, K. B. Crozier, S. R. Manalis, S. C. Minne, K. Wilder, G. S. Kino, and C. F. Quate, *Appl. Phys. Lett.* **74**(4), 501–503 (1999).
- <sup>13</sup>S. M. Mansfield and G. S. Kino, *Appl. Phys. Lett.* **57**(24), 2615–2616 (1990).
- <sup>14</sup>Y. B. Duan, G. Barbastathis, and B. L. Zhang, *Opt. Lett.* **38**(16), 2988–2990 (2013).
- <sup>15</sup>R. Ye, Y. H. Ye, H. F. Ma, L. L. Cao, J. Ma, F. Wyrowski, R. Shi, and J. Y. Zhang, *Sci. Rep.* **4**, 3769 (2014).
- <sup>16</sup>L. Novotny and B. Hecht, *Principles of Nano-Optics*, 2nd ed. (Cambridge University Press, Cambridge, 2012).
- <sup>17</sup>A. J. den Dekker and A. van den Bos, *J. Opt. Soc. Am. A* **14**(3), 547–557 (1997).
- <sup>18</sup>Q. W. Zhan, *Adv. Opt. Photonics* **1**(1), 1–57 (2009).
- <sup>19</sup>S. Quabis, R. Dorn, M. Eberler, O. Glockl, and G. Leuchs, *Opt. Commun.* **179**(1–6), 1–7 (2000).
- <sup>20</sup>G. Chartier, *Introduction to Optics* (Springer, New York, 2005).